Shapiro steps and stability of skyrmions interacting with alternating anisotropy under the influence of ac and dc drives

J. C. Bellizotti Souza,[1] N. P. Vizarim,[2] C. J. O. Reichhardt,[3] C. Reichhardt,[3] and P. A. Venegas[4]

[1]*POSMAT—Programa de Pós-Graduação em Ciência e Tecnologia de Materiais, São Paulo State University (UNESP), School of Sciences, Bauru 17033-360, SP, Brazil*

[2]*Departament of Electronics and Telecommunications Engineering, São Paulo State University (UNESP), School of Engineering, São Jõao da Boa Vista 13876-750, SP, Brazil*

[3]*Theoretical Division and Center for Nonlinear Studies, Los Alamos National Laboratory, Los Alamos, New Mexico 87545, USA*

[4]*Department of Physics, São Paulo State University (UNESP), School of Sciences, Bauru 17033-360, SP, Brazil*

(Received 22 April 2024; accepted 20 June 2024; published 3 July 2024)

We use atomistic simulations to examine the sliding dynamics of a skyrmion in a two-dimensional system containing a periodic one-dimensional stripe pattern of variations between low and high values of the perpendicular magnetic anisotropy. The skyrmion changes in size as it crosses the interface between two anisotropy regions. On applying combined dc and ac driving in either parallel or perpendicular directions, we observe a wide variety of Shapiro steps, Shapiro spikes, and phase-locking phenomena. The phase-locked orbits have two-dimensional dynamics due to the gyrotropic or Magnus dynamics of the skyrmions and are distinct from the phase-locked orbits found for strictly overdamped systems. Along a given Shapiro step when the ac drive is perpendicular to the dc drive, the velocity parallel to the ac drive is locked while the velocity in the perpendicular direction increases with increasing drive to form Shapiro spikes. At the transition between adjacent Shapiro steps, the parallel velocity jumps up to the next step value, and the perpendicular velocity drops. The skyrmion Hall angle shows a series of spikes as a function of increasing dc drive, where the jumps correspond to the transition between different phase-locked steps. At high drives, the Shapiro steps and Shapiro spikes are lost. When both the ac and dc drives are parallel to the stripe periodicity direction, Shapiro steps appear, while if the dc drive is parallel to the stripe periodicity direction and the ac drive is perpendicular to the stripe periodicity, then there are only two locked phases, and the skyrmion motion consists of a combination of sliding along the interfaces between the two anisotropy values and jumping across the interfaces.

DOI: 10.1103/PhysRevB.110.014406

I. INTRODUCTION

Complex systems in the presence of multiple interacting frequencies exhibit a range of nonlinear dynamical phenomena, including synchronization and phase locking [1,2]. These phenomena appear across diverse domains, from interconnected pendula [3] to biological systems [4]. A fundamental illustration of phase locking occurs in overdamped particle systems traversing a periodic substrate under simultaneous direct (dc) and alternating (ac) driving forces. In this case, resonances can occur between the ac driving frequency and the oscillation frequency induced by the particle motion across the substrate. These resonant interactions result in distinct steps in the velocity-force curves, since the particle remains locked to a specific velocity range over a range of external drive intervals in order to sustain the resonant state. These resonant steps were initially observed in Josephson junctions, where the current-voltage response exhibits what are called Shapiro steps [5,6]. Many systems demonstrating phase locking can be modeled as effectively one-dimensional (1D) in nature, such as Josephson junction arrays [7], incommensurate sliding charge density waves [8–10], superconducting vortices on 1D [11–13] and 2D periodic substrates [14,15], driven Frenkel-Kontorova models [16], frictional systems [17], and colloids navigating 1D periodic substrates [18–20]. Even within one-dimensional systems, several additional phenomena, such as fractional locking, can arise when additional nonlinear effects are considered.

For the case of particles moving over a 2D periodic substrate, many of the same types of phase locking effects observed in 1D systems can occur; however, the additional degrees of freedom in the 2D environment make it possible to observe new types of effects by, for example, applying the ac drive in a direction that is perpendicular to the dc drive. Such a driving configuration produces transverse phase locking that is distinct from Shapiro steps. The widths of the transverse locking steps generally increase with increasing ac amplitude [21,22], unlike the oscillatory behavior observed for Shapiro steps. For 2D substrates, it is also possible to apply biharmonic ac driving with components that are both parallel and perpendicular to the dc drive in order to induce circular motion of the driven particles. In this scenario, increasing the dc drive intensity leads to chiral scattering effects, resulting in phase-locked regions where the particles move both parallel and perpendicular to the dc driving direction [23,24].

In most of the previously mentioned systems, the dynamics are predominantly overdamped; however, under certain circumstances, nondissipative effects such as inertia become

 ©2024 American Physical Society

important [25]. Another possible nondissipative term is produced by gyro-coupling or the Magnus force, which generates velocity components perpendicular to the forces acting on the particle. In a 1D system, the Magnus force remains negligible, but in 2D systems, it can significantly alter the dynamics. An important and recent example of a system in which the gyromagnetic forces are dominant are magnetic skyrmions in ferromagnets. Magnetic skyrmions are topologically protected magnetic textures [26,27] that exhibit many similarities to overdamped particles. Skyrmions can minimize their repulsive interactions by forming a triangular lattice, can be set in motion by the application of external drives, and can interact with material defects in several different ways [28–30]. Under external driving in a clean sample, skyrmions move at an angle to the applied drive that is known as the intrinsic skyrmion Hall angle $\theta_{\rm sk}^{\rm int}$ [26,31–35] with respect to the external drive. The sign of this angle depends on the skyrmion winding number Q [26,31–37]. The existence of a finite skyrmion Hall angle is an issue for technological applications, since it can cause skyrmions to move towards the sample edge and be annihilated, leading to data loss in the skyrmion-based device. In order to prevent this, there have been extensive studies on ways to precisely control the skyrmion motion. Methods proposed to mitigate the skyrmion Hall angle, or to take advantage of some of its proprieties, include periodic pinning [38–43], sample curvature [44–46], interface guided motion [47,48], ratchet effects [49–53], temperature and magnetic field gradients [54–57], granular films [58,59], parametric pumping [60], voltage-controlled perpendicular magnetic anisotropy (PMA) [61,62], skyrmion-vortex coupling using heterostructures [63,64], skyrmion lattice compression [65,66], laminar flow of skyrmions [67], soliton motion along skyrmion chains [68,69], pulse current modulation [70], strain driven motion [71], and motion by interacting with domain walls [72].

Recent investigations into the interaction of skyrmions with both dc and ac driving have aimed at elucidating the impact of the Magnus effect on Shapiro steps. Reichhardt and Reichhardt [73] demonstrated that the presence of the Magnus force caused a shift of the locking steps to higher dc drives. Additionally, when a longitudinal dc drive was combined with a transverse ac drive, they observed pronounced Shapiro steps corresponding to intricate 2D periodic orbits that cannot be replicated using overdamped particles. In a subsequent study [74], Reichhardt and Reichhardt also identified the occurrence of Shapiro spikes as well as negative mobility, where the skyrmions move in the direction opposite to the dc driving direction. More recently, Vizarim *et al.* [75] found that significant skyrmion Hall angle overshoots and reversals can occur under certain conditions. Although these observations offer valuable insights into the behavior of skyrmions under simultaneous dc and ac driving, it is worth noting that these simulations were conducted using a particle-based model [34] that does not account for skyrmion annihilation, creation, or deformations such as internal excitations. Consequently, a more detailed and realistic study of the structural and dynamic behavior of skyrmions under ac and dc driving conditions is still lacking.

In this work, using atomistic simulations, we investigate the dynamical behavior of a single skyrmion subjected to a combination of external ac and dc driving while interacting with a quasi-one-dimensional array of defects that form a stripe pattern along the x direction, as illustrated in Fig. 1. In experiments, this periodic array of stripe patterns could be reproduced using voltage-controlled magnetic anisotropy (VCMA) [76,77]. We find that when the ac drive is applied in the y direction and the dc drive is applied in the x direction, velocity steps appear in which the x velocity remains constant with increasing dc drive, as in ordinary Shapiro steps, while the y velocity magnitude increases. The amplitude of the ac drive determines the number of Shapiro steps that appear, with higher ac amplitudes giving more Shapiro steps. This behavior changes above a saturation value of the dc drive, when the combination of the ac and dc driving becomes so strong that no Shapiro steps can form and the effect of varying the skyrmion size becomes minimal. We also investigate the dynamical response when a fixed dc drive is applied along the y direction and an ac drive of increasing amplitude is applied in either the x or y direction. When both drives are in the x direction, we find a regime in which both the x and y velocities exhibit a series of constant velocity steps separated by velocity dips. Our results should be useful for spintronics devices where precise control of the skyrmion velocity and angle of motion are required.

II. SIMULATION

We consider an ultrathin ferromagnetic sample that is capable of hosting Néel skyrmions. The sample has dimensions of 272 × 136 nm and we apply periodic boundary conditions along the x and y directions. A magnetic field is applied perpendicular to the sample surface along the positive z direction at zero temperature, $T = 0$ K. The PMA takes high and low values in periodic stripes that extend along the y direction and vary along the x direction, as illustrated in Fig. 1(a). In this work we consider the dynamics of a single skyrmion under the influence of both dc and ac driving starting from the initial configuration shown in Fig. 1(a).

The simulations are performed using the atomistic model [78], which captures the dynamics of individual atomic magnetic moments. This method enables us to investigate the spin texture dynamics in detail. The Hamiltonian governing the atomistic dynamics is given in Refs. [32,78,79]:

$$\begin{aligned}\mathcal{H} = &-\sum_{i,j\in N} J_{i,j}\mathbf{m}_i\cdot\mathbf{m}_j - \sum_{i,j\in N}\mathbf{D}_{i,j}\cdot\left(\mathbf{m}_i\times\mathbf{m}_j\right)\\ &-\sum_i \mu\mathbf{H}\cdot\mathbf{m}_i - \sum_{i\in R_L} K_L(\mathbf{m}_i\cdot\hat{\mathbf{z}})^2\\ &-\sum_{i\in R_H} K_H(\mathbf{m}_i\cdot\hat{\mathbf{z}})^2. \end{aligned} \tag{1}$$

The underlying lattice is a square arrangement of spins with lattice constant $a = 0.5$ nm. The first term on the right side is the exchange interaction between the nearest neighbors contained in the set N, with an exchange constant of $J_{i,j}$ between magnetic moments i and j. The second term is the interfacial Dzyaloshinskii-Moriya interaction, where $\mathbf{D}_{i,j}$ is the Dzyaloshinskii-Moriya vector between magnetic moments i and j. The third term is the Zeeman interaction with an

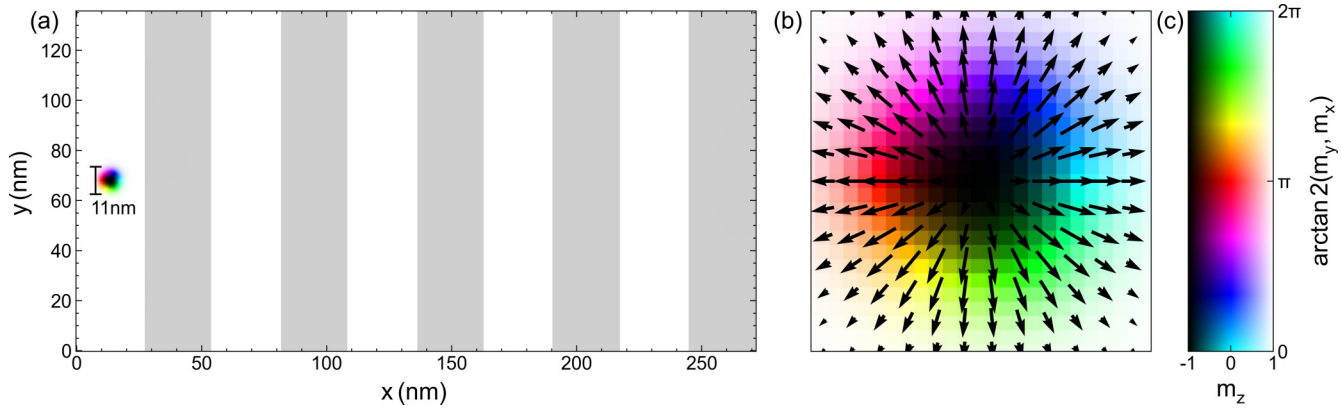

FIG. 1. (a) Illustration of the sample used throughout this work. Regions with low PMA of $K_L = 0.02J$ are colored white and regions with high PMA of $K_H = 0.05J$ are colored gray. We use this anisotropy color representation throughout the work. The skyrmion starts at the center left edge of the sample, as shown, and has a diameter of approximately $\xi = 11$ nm for $D/J = 0.18$. (b) Blow up showing the atomic moments that form the Néel skyrmion. (c) Illustration of the color wheel used in this work. Positive out-of-plane magnetic moments are white and negative out-of-plane magnetic moments are black. Values in between these two limits are colored according to the angle between m_x and m_y.

applied external magnetic field $\mathbf{H}$. Here $\mu = \hbar\gamma$ is the magnitude of the magnetic moment and $\gamma = 1.76 \times 10^{11}\ \mathrm{T}^{-1}\,\mathrm{s}^{-1}$ is the electron gyromagnetic ratio. The last two terms represent the PMA of the sample. K_L is the anisotropy constant for low-anisotropy regions contained in the set R_L, and K_H is the anisotropy constant for high-anisotropy regions contained in the set R_H. Since we are considering ultrathin films, long-range dipolar interactions can be neglected because they are expected to be very small [80].

The time evolution for the individual atomic magnetic moments is given by the LLGS equation [81–83]:

$$\frac{\partial \mathbf{m}_i}{\partial t} = -\gamma \mathbf{m}_i \times \mathbf{H}_i^{\mathrm{eff}} + \alpha \mathbf{m}_i \times \frac{\partial \mathbf{m}_i}{\partial t} + \frac{pa^3}{2e}(\mathbf{j}\cdot\nabla)\mathbf{m}_i. \quad (2)$$

Here γ is the electron gyromagnetic ratio, $\mathbf{H}_i^{\mathrm{eff}} = -\frac{1}{\hbar\gamma}\frac{\partial \mathcal{H}}{\partial \mathbf{m}_i}$ is the effective magnetic field, including all interactions from the Hamiltonian, α is the phenomenological damping introduced by Gilbert, and the last term is the adiabatic spin-transfer-torque (STT), where p is the spin polarization, e the electron charge, and $\mathbf{j}$ the applied current density. Use of this STT expression implies that the conduction electron spins are always parallel to the magnetic moments $\mathbf{m}$ [32,84]. The nonadiabatic terms can be neglected in this case, since they do not affect the skyrmion dynamics significantly under small driving forces [31]. The current density $\mathbf{j}$ used in this work has the form:

$$\mathbf{j} = j_{\mathrm{ac}}[\cos(2\pi f t)\hat{\mathbf{x}} + \sin(2\pi f t)\hat{\mathbf{y}}]\cdot\hat{\mathbf{d}}_{\mathrm{ac}} + j_{\mathrm{dc}}\hat{\mathbf{d}}_{\mathrm{dc}}, \quad (3)$$

where the oscillation frequency f is fixed at $f = 50.6 \times 10^6$ Hz, t is the time, and $\hat{\mathbf{d}}_{\mathrm{dc}}$ and $\hat{\mathbf{d}}_{\mathrm{ac}}$ are the directions of the applied dc and ac currents, respectively.

The skyrmion velocity is computed using the emergent electromagnetic fields [81,85]:

$$E_i^{\mathrm{em}} = \frac{\hbar}{e}\mathbf{m}\cdot\left(\frac{\partial \mathbf{m}}{\partial i}\times\frac{\partial \mathbf{m}}{\partial t}\right), \quad (4)$$

$$B_i^{\mathrm{em}} = \frac{\hbar}{2e}\varepsilon_{ijk}\mathbf{m}\cdot\left(\frac{\partial \mathbf{m}}{\partial j}\times\frac{\partial \mathbf{m}}{\partial k}\right), \quad (5)$$

where ε_{ijk} is the totally antisymmetric tensor. The skyrmion drift velocity, $\mathbf{v}_d$, is then calculated using $\mathbf{E}^{\mathrm{em}} = -\mathbf{v}_d \times \mathbf{B}^{\mathrm{em}}$. Our simulation uses fixed values of $\mu\mathbf{H} = 0.5(D^2/J)\hat{\mathbf{z}}$, $\alpha = 0.3$, and $p = -1.0$. The material parameters, unless otherwise specified, are $J = 1$ meV, $D = 0.18J$, $K_L = 0.02J$, and $K_H = 0.05J$. These material parameters stabilize Néel skyrmions similar to those found for Pt/Co/MgO thin films [86]. In other materials, the exchange constant J may be different; however, since all units are normalized by J, our results remain valid after appropriate rescaling of the measurements. For each simulation, the system starts in the initial configuration illustrated in Fig. 1(a). The numerical integration of Eq. (2) is performed using a fourth-order Runge-Kutta method. For each value of j_{ac} and j_{dc}, we calculate the time average skyrmion velocity components, $\langle v_x\rangle$ and $\langle v_y\rangle$, over 3×10^7 time steps to ensure a steady state.

III. DC DRIVE ALONG *x* AND AC DRIVE ALONG *y*

We begin our analysis with a system in which the ac drive is applied along the y direction and the dc drive is applied along the x direction, giving $\hat{\mathbf{d}}_{\mathrm{ac}} = \hat{\mathbf{y}}$ and $\hat{\mathbf{d}}_{\mathrm{dc}} = \hat{\mathbf{x}}$. We fix $j_{\mathrm{ac}} = 5 \times 10^{10}\ \mathrm{A\,m^{-2}}$ and vary j_{dc} over the range $1 \times 10^{10}\ \mathrm{A\,m^{-2}} \leqslant j_{\mathrm{dc}} \leqslant 8 \times 10^{10}\ \mathrm{A\,m^{-2}}$.

In Fig. 2 we plot the average velocities $\langle v_x\rangle$ and $\langle v_y\rangle$ along with the skyrmion Hall angle $\theta_{\mathrm{sk}} = \arctan(\langle v_y\rangle/\langle v_x\rangle)$ as a function of j_{dc}. Here $\langle v_x\rangle$ exhibits constant velocity steps similar to the Shapiro steps that appear when the ac and dc drives are both applied in the same direction. In overdamped systems, when the ac and dc drives are both aligned along the x direction, velocity steps appear in the x direction but there are no steps in the y direction since there is no net drift along y; however, the skyrmions have a finite velocity response in both the x and y directions due to the gyrotropic force. The steps in $\langle v_x\rangle$ in Fig. 2(a) span a wide range of j_{dc}, and over this same range, Fig. 2(b) indicates that the skyrmion Hall angle has a nonmonotonic behavior. For the Shapiro steps to exist, the dc drive must exceed a depinning threshold in order to induce motion along the $+x$ direction. In this system, the

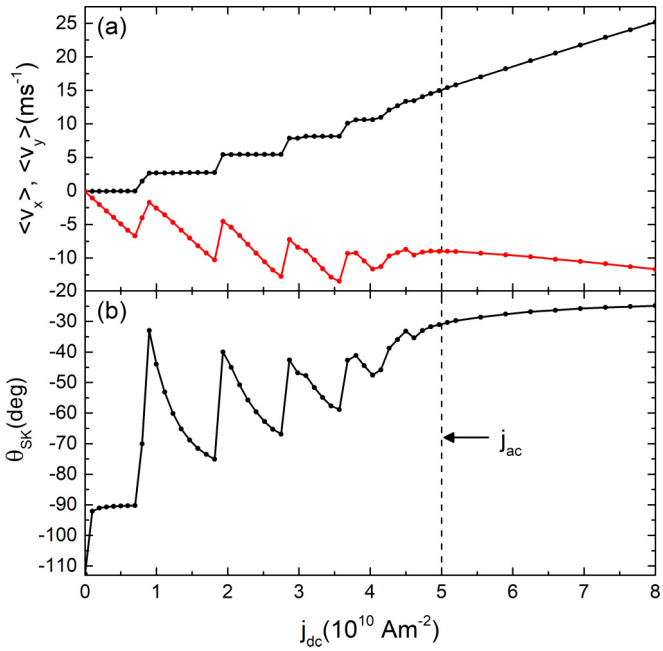

FIG. 2. A sample with y direction ac driving and x direction dc driving where $j_{ac} = 5 \times 10^{10}$ A m^{-2} and $D/J = 0.18$. (a) The average skyrmion velocities $\langle v_x \rangle$ (black) and $\langle v_y \rangle$ (red) vs j_{dc}. (b) The corresponding skyrmion Hall angle θ_{sk} vs j_{dc}. The vertical dashed line indicates the value of j_{dc} at which $j_{dc} = j_{ac}$.

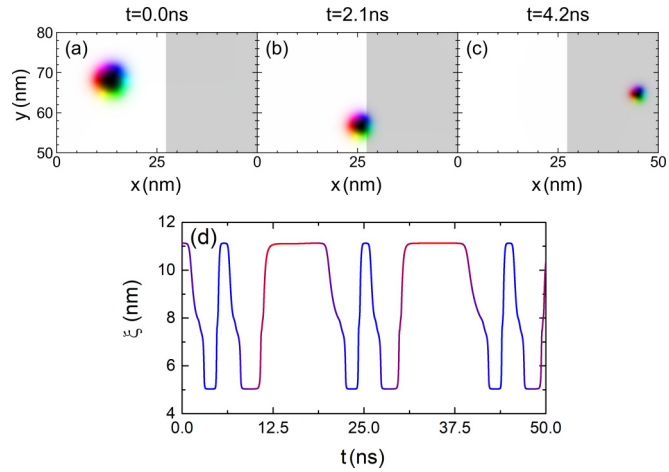

FIG. 3. Snapshots of the skyrmion texture and time evolution of the skyrmion diameter while approaching and interacting with a region (gray) of stronger PMA for the system from Fig. 2 with y direction ac driving and x direction dc driving at $j_{dc} = 2.52 \times 10^{10}$ A m^{-2}, $j_{ac} = 5.00 \times 10^{10}$ A m^{-2}, and $D/J = 0.18$. (a) At $t = 0$ ns, the skyrmion is inside the low-anisotropy region R_L, and has its normal diameter of $\xi \approx 11$ nm. (b) At $t = 2.1$ ns, as the skyrmion approaches the interface between regions with different PMA, it shrinks to $\xi \approx 8$ nm. (c) At $t = 4.2$ ns, when the skyrmion is inside region R_H with high anisotropy, $\xi \approx 5$ nm. (d) The skyrmion diameter ξ as a function of time t as it moves and crosses the multiple interfaces along the sample. ξ varies as a gradient from blue to red corresponding to the $+y$ and $-y$ portions of the ac drive, respectively.

dc threshold is $j_{dc} = 1.93 \times 10^{10}$ A m^{-2}. This value can be modified depending on the PMA values used in the system: higher K_H results in higher depinning currents, while lower K_H results in lower depinning currents. Along a given constant $\langle v_x \rangle$ step, such as the step appearing for 1.93×10^{10} A m^{-2} $< j_{dc} < 2.75 \times 10^{10}$ A m^{-2}, the magnitude of $\langle v_y \rangle$ increases linearly with increasing j_{dc}. As a consequence, θ_{sk} becomes significantly more negative, meaning that the direction of the skyrmion flow changes as j_{dc} increases along the velocity step. When a new velocity step is reached and the value of $\langle v_x \rangle$ changes, there is a pronounced jump in $\langle v_y \rangle$ to a value that is smaller in magnitude. As j_{dc} increases along this new step, the magnitude of $\langle v_y \rangle$ increases linearly again until the next step is reached and the process repeats. The velocity steps are associated with Shapiro step phase locking, where there is a matching of the ac drive frequency or its higher harmonics to the frequency of the skyrmion velocity oscillations produced by the periodic encounters with the higher-anisotropy regions, R_H. These regions are spaced periodically across the sample and act as slightly repulsive barriers to the skyrmion motion. Shapiro steps have been observed previously for skyrmions [73–75]; however, the present work marks the first observation of skyrmion Shapiro steps using a detailed atomistic model, which proves that the skyrmion structure remains stable across the steps.

In Fig. 3 we show snapshots of the skyrmion structure as it passes between regions with different PMA. The skyrmion has a normal size in region R_L, but in region R_H the skyrmion size is strongly reduced. During the transition between regions, the skyrmion size changes smoothly. This size variation as the skyrmion traverses regions with different PMA is in agreement with the results of Refs. [61,62]. In the Supplemental Material [87], we provide a movie of the skyrmion transition illustrated in Figs. 3(a)–3(c). The Shapiro step behavior persists until $j_{dc} \approx j_{ac}$, when both velocity components begin to increase linearly in magnitude with increasing j_{dc} and the steplike behavior of $\langle v_x \rangle$ is lost. Note that as j_{dc} approaches j_{ac}, the sharpness of the Shapiro steps decreases. The steps are most clearly visible when j_{dc} is small relative to j_{ac}. In Fig. 2(b), the behavior of θ_{sk} is similar to that of $\langle v_y \rangle$. The increase in magnitude of the skyrmion Hall angle value along a given step in $\langle v_x \rangle$ is not linear but takes the form $\theta_{sk} = \arctan(\langle v_y \rangle / \langle v_x \rangle)$ where $\langle v_y \rangle$ increases while $\langle v_x \rangle$ is constant.

In Fig. 4 we illustrate some selected skyrmion trajectories for the system from Fig. 2. At $j_{dc} = 1.47 \times 10^{10}$ A m^{-2} in Fig. 4(a), the x direction skyrmion velocity is constant at $\langle v_x \rangle \approx 2.7$ m s^{-1}. During the $+y$ portion of the ac drive cycle (blue line), the skyrmion moves mainly along the $+x$ and $+y$ directions, and it can traverse exactly two stripes with different PMA values. In the $-y$ portion of the ac drive cycle (red line), the skyrmion remains within the low-anisotropy region and moves mainly along the $-y$ direction. In the Supplemental Material [87], we show the skyrmion trajectory in a short movie. In Fig. 4(b) at $j_{dc} = 2.52 \times 10^{10}$ A m^{-2}, $\langle v_x \rangle \approx 5.4$ m s^{-1} and the system is on the second Shapiro step. Here during the $+y$ portion of the ac cycle the skyrmion traverses four stripes, while the $-y$ motion that appears during the $-y$ portion of the ac cycle follows nearly straight lines. For $j_{dc} = 3.45 \times 10^{10}$ A m^{-2} where $\langle v_x \rangle \approx 8.1$ m s^{-1}, Fig. 4(c) shows that the skyrmion traverses five stripes during

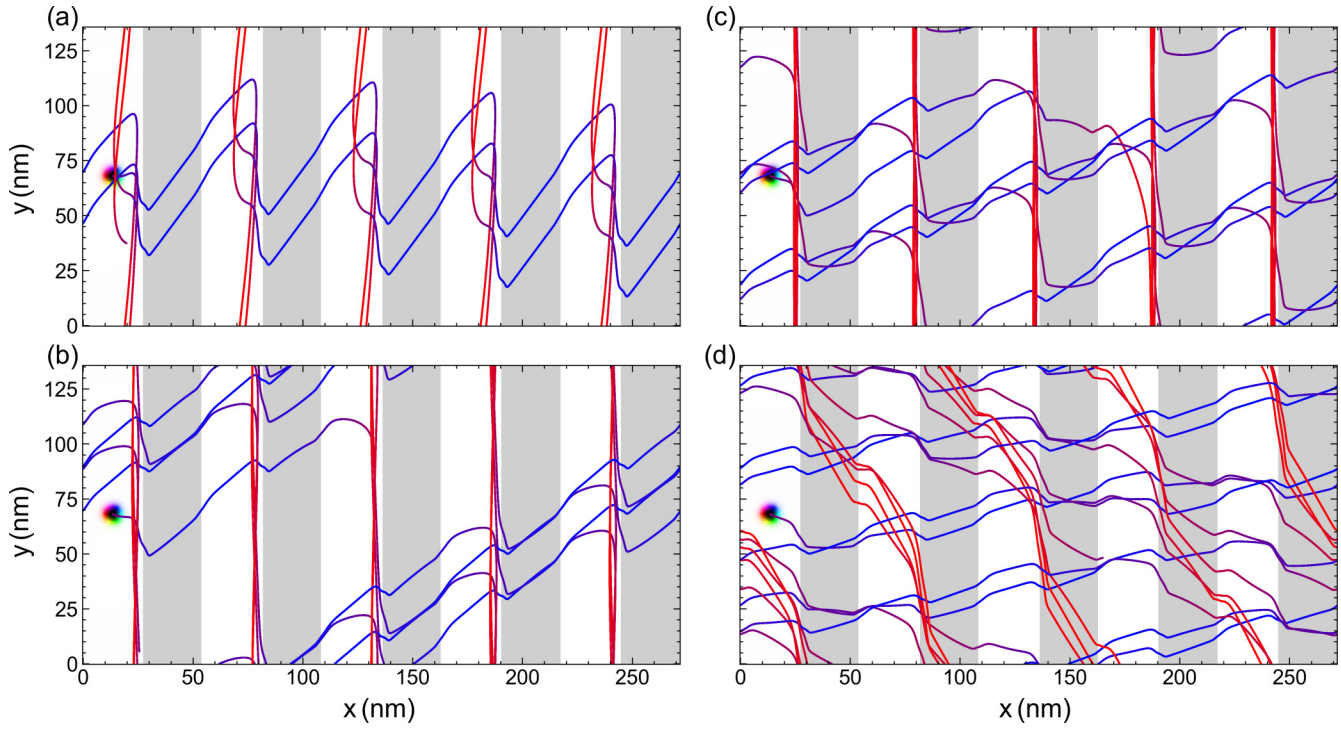

FIG. 4. Skyrmion trajectories for the system from Fig. 2 with y direction ac driving and x direction dc driving at $j_{ac} = 5.00 \times 10^{10}$ A m^{-2} and $D/J = 0.18$. The trajectory color varies as a gradient from blue to red corresponding to the $+y$ and $-y$ portion of the ac driving cycle, respectively. White stripes represent lower-anisotropy regions and gray stripes indicate higher-anisotropy regions. (a) $j_{dc} = 1.47 \times 10^{10}$ A m^{-2}. (b) $j_{dc} = 2.52 \times 10^{10}$ A m^{-2}. (c) $j_{dc} = 3.45 \times 10^{10}$ A m^{-2}. (d) $j_{dc} = 5.90 \times 10^{10}$ A m^{-2}.

the $+y$ portion of the ac cycle. Finally, when the magnitude of the dc drive is greater than that of the ac drive, as shown in Fig. 4(d) for $j_{dc} = 5.90 \times 10^{10}$ A m^{-2}, the skyrmion can traverse multiple stripes during both the $+y$ and $-y$ portions of the ac drive cycle. This destroys the resonance between the ac drive and the collisions between the skyrmion and the R_H regions and therefore extinguishes the Shapiro step behavior. In the Supplemental Material [87], we provide a short movie illustrating the skyrmion trajectory.

One common dynamical behavior observed for all values of j_{dc} that fall along a step in $\langle v_x \rangle$ is that when the skyrmion approaches the interface between regions R_L and R_H, it is repelled by the higher-anisotropy region. The R_H region thus acts like a repulsive potential barrier for the skyrmion motion. The skyrmion can only cross this barrier if it receives enough energy from the applied drives to modify its internal structure in order to shrink and enter the higher-anisotropy region, as illustrated in Fig. 3. When the ability of the skyrmion to shrink is curtailed by insufficient available energy from the drive, so that the skyrmion remains trapped in the lower-anisotropy region, the repulsive interaction causes the skyrmion to slide close to the $R_L - R_H$ interface, giving rise to a Magnus velocity boost of the type observed in previous works [66,88,89]. This behavior can be observed in Figs. 4(a), 4(b) and 4(c). During the $+y$ portion of the ac cycle, the force from the ac drive is rotated by the Magnus term to produce a skyrmion velocity component along a diagonal from lower left to upper right. At the same time, the dc driving force that is applied along the $+x$ direction generates a Magnus velocity component along a diagonal from upper left to lower right. When both Magnus components are combined, the net result is a relatively large velocity in the $+x$ direction. This combination provides sufficient energy to shrink the skyrmion and allow it to transport across the interface. In contrast, during the $-y$ portion of the ac cycle, the Magnus force component from the ac drive is oriented diagonally from the upper right to the lower left. When this motion combines with the Magnus term from the dc drive, the $-y$ motion of the skyrmion is enhanced, while the $+x$ motion is diminished, resulting in insufficient energy for the skyrmion to deform and cross the interface.

A. Varying the ac amplitude

We next explore the impact of the ac drive amplitude on the dynamical behavior by considering four different values of j_{ac}: $j_{ac} = 2 \times 10^{10}$Am^{-2}, 3×10^{10}Am^{-2}, 4×10^{10}Am^{-2}, and 5×10^{10}Am^{-2}. In Fig. 5 we plot the skyrmion average velocities $\langle v_x \rangle$ and $\langle v_y \rangle$ as a function of the dc drive amplitude j_{dc} for each of these ac drive values. In every case there is a range of j_{dc} over which well-defined velocity Shapiro steps appear in $\langle v_x \rangle$. On these steps, $\langle v_y \rangle$ increases linearly in magnitude, and sudden jumps in $\langle v_y \rangle$ appear on transitioning from one $\langle v_x \rangle$ step to another. The number of steps that can form is determined by the ac drive amplitude, with higher amplitudes favoring the appearance of Shapiro steps and lower amplitudes hindering step formation. The range of j_{dc} values for which the Shapiro steps can be observed, which also determines how many steps are present, is given by $j_{dc} \leqslant j_{ac}$. This indicates that Shapiro steps for skyrmion

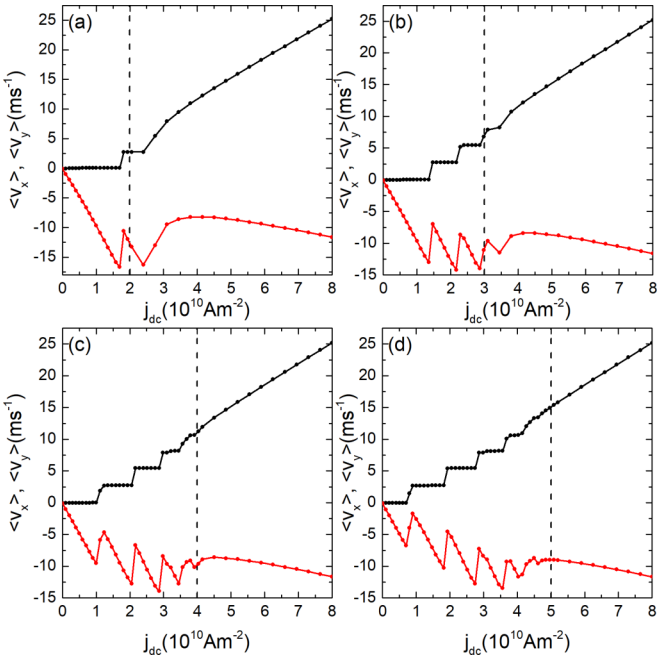

FIG. 5. $\langle v_x \rangle$ (black) and $\langle v_y \rangle$ (red) vs j_{dc} in samples with y direction ac driving and x direction dc driving where $D/J = 0.18$. (a) $j_{ac} = 2 \times 10^{10}$ A m^{-2}. (b) $j_{ac} = 3 \times 10^{10}$ A m^{-2}. (c) $j_{ac} = 4 \times 10^{10}$ A m^{-2}. (d) $j_{ac} = 5 \times 10^{10}$ A m^{-2}. The vertical dashed lines indicate the value of j_{ac} at which $j_{ac} = j_{dc}$.

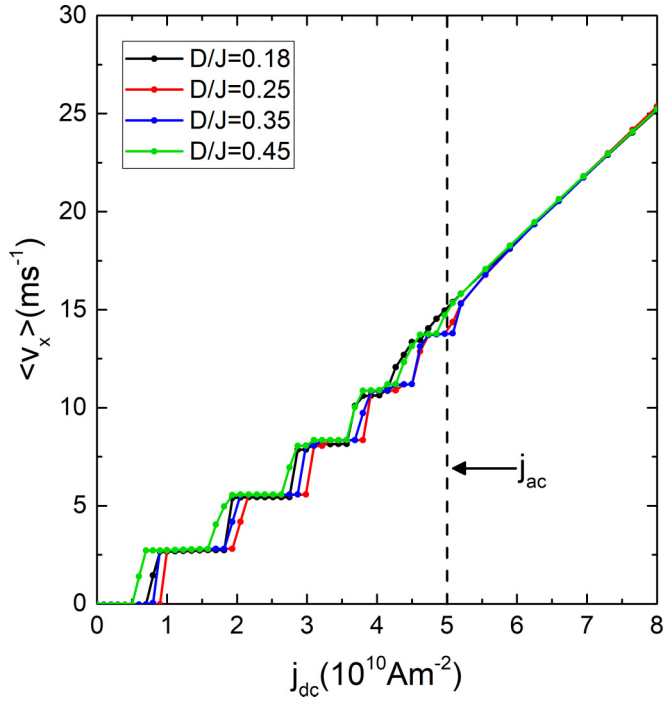

FIG. 6. $\langle v_x \rangle$ vs j_{dc} for $D/J = 0.18$ (black), $D/J = 0.25$ (red), $D/J = 0.35$ (blue), and $D/J = 0.45$ (green) in samples with y direction ac driving, x direction dc driving, and fixed $j_{ac} = 5 \times 10^{10}$ A m^{-2}. The dashed line indicates the point at which $j_{ac} = j_{dc}$.

systems should remain robustly observable for a wide range of ac and dc drive amplitudes.

B. The influence of D/J

In skyrmion systems, the ratio D/J of magnetic parameters is responsible for determining the size and stability of the skyrmion [37]. Thus, we can investigate the effects of different skyrmion sizes on the Shapiro steps by varying the ratio D/J. In Fig. 6 we plot the average skyrmion velocity $\langle v_x \rangle$ as a function of the dc drive intensity j_{dc} for fixed $j_{ac} = 5 \times 10^{10}$ A m^{-2} and different values of D/J. We find that Shapiro velocity steps are present for all values of D/J, indicating that Shapiro step behavior is robust in this system. As D/J increases, the Dzyaloshinskii-Moriya interaction becomes stronger than the exchange interaction, leading to a reduction in the skyrmion size. The consequences of changing the skyrmion size are subtle, and we find that the velocity-current curves can be shifted towards higher or lower values of j_{dc} depending on the value of D/J. The number and width of the Shapiro steps are very similar for the D/J values simulated here, but we find that as D/J increases, the transitions between the Shapiro steps become smoother. For lower values of D/J, the transitions are sharper and well defined, whereas for larger D/J values, transient regions emerge between the constant velocity steps. This may be the result of a reduced contrast in the size of the skyrmion as it moves between the low- and high-PMA regions when the skyrmion becomes smaller. We expect that for very high values of D/J, the transient effects may become dominant and the Shapiro steps would be lost.

In Fig. 7 we illustrate the skyrmion trajectories at fixed $j_{dc} = 2.05 \times 10^{10}$ A m^{-2} and $j_{ac} = 5 \times 10^{10}$ A m^{-2} for different values of D/J. Focusing on the $+y$ portion of the ac cycle, we find that the skyrmion with $D/J = 0.18$ in Fig. 7(a) can traverse approximately two and a half stripes during this time period. In Fig. 7(b) for $D/J = 0.25$, the skyrmion is smaller and it traverses only two stripes. For $D/J = 0.35$ in Fig. 7(c), the skyrmion becomes even smaller but it returns to traveling approximately two and a half stripes. Finally, for $D/J = 0.45$ in Fig. 7(d), the very small skyrmion traverses three stripes. Although the dynamics change in a nontrivial way, in each case we find a common behavior: The skyrmion is able to move from a low-anisotropy region to a high-anisotropy region only during the $+y$ portion of the ac cycle. This is the same behavior described in Fig. 4, where the Magnus force components from the ac and dc drives must combine in the right way to allow the skyrmion to overcome the effective potential barrier at the $R_L - R_H$ interface.

IV. AC AND DC DRIVES IN DIFFERENT CONFIGURATIONS

To this point, we have only considered systems where the ac drive was applied along the y direction and the dc drive was applied along the $+x$ direction. It is, however, known that other combinations of ac and dc driving can produce interesting particle dynamics [49,73–75]. Thus, we next consider the effect of the external drive directions on the skyrmion dynamics. We investigate two combinations: (i) ac drive applied along the x direction and dc drive applied along the $+y$ direction, $\hat{\mathbf{d}}_{ac} = \hat{\mathbf{x}}$ and $\hat{\mathbf{d}}_{dc} = \hat{\mathbf{y}}$, and (ii) ac and dc drives applied along the x direction, $\hat{\mathbf{d}}_{ac} = \hat{\mathbf{d}}_{dc} = \hat{\mathbf{x}}$. In both cases, we fix the external dc drive at $j_{dc} = 4 \times 10^{10}$ A m^{-2} and vary

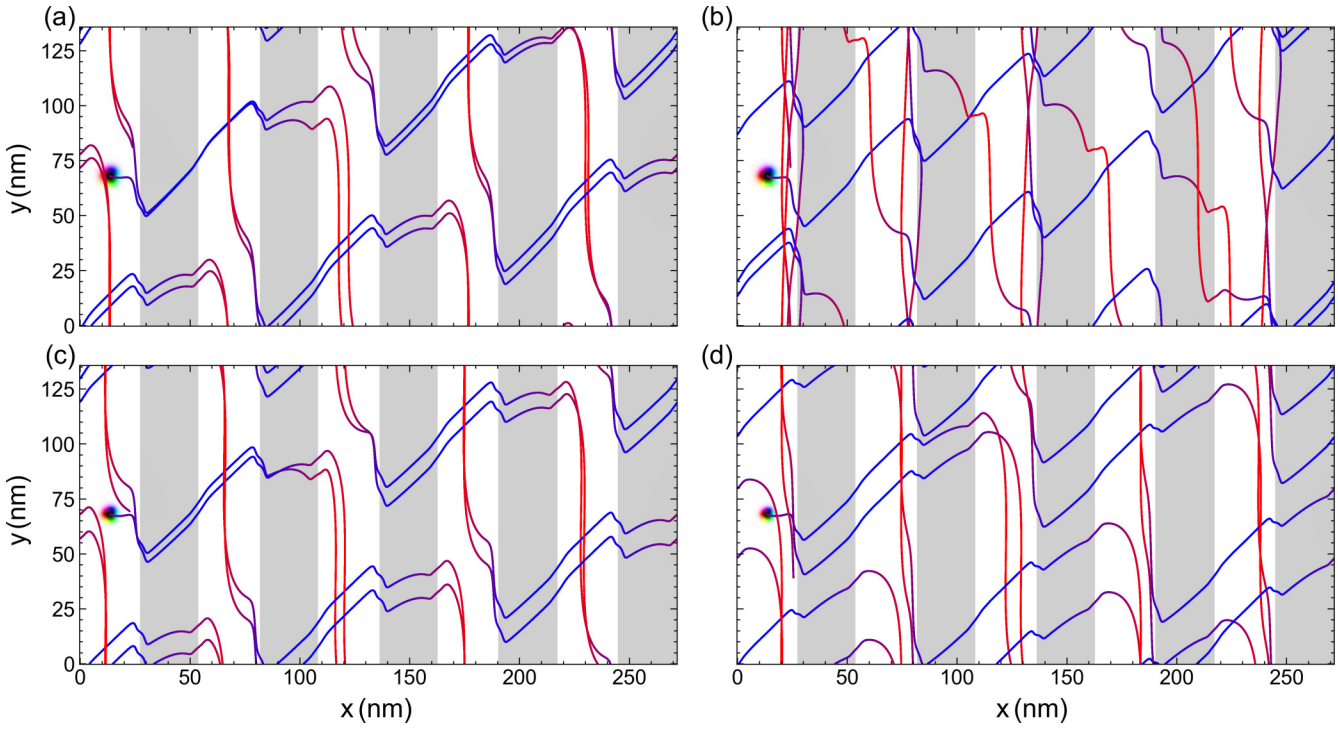

FIG. 7. Skyrmion trajectories for the system from Fig. 6 with y direction ac driving and x direction dc driving at $j_{dc} = 2.05 \times 10^{10}$ A m^{-2} and $j_{ac} = 5 \times 10^{10}$ A m^{-2}. The trajectory color varies as a gradient from blue to red corresponding to the $+y$ and $-y$ portion of the ac driving cycle, respectively. White stripes represent lower-anisotropy regions and gray stripes indicate higher-anisotropy regions. Note that for each value of D/J, the skyrmion diameter ξ is slightly different. (a) $D/J = 0.18$ and $\xi = 11.0$ nm. (b) $D/J = 0.25$ and $\xi = 10.8$ nm. (c) $D/J = 0.35$ and $\xi = 9.3$ nm. (d) $D/J = 0.45$ and $\xi = 7.8$ nm.

the ac drive amplitude j_{ac}. Note that this is the opposite to the protocol used in Sec. III, where the dc drive was varied while the ac drive amplitude was held fixed.

In Fig. 8(a) we plot $\langle v_x \rangle$ and $\langle v_y \rangle$ as a function of j_{ac} when the ac drive is applied along the x direction and the dc drive is applied along the $+y$ direction. In the absence of an ac drive, although the y direction dc drive would produce a component of skyrmion motion along the x direction due to the Magnus term, this component is not large enough to push the skyrmion across the barrier at the $R_L - R_H$ interface, and the skyrmion would remain in the low-anisotropy region. When a finite x direction ac drive is added, however, the skyrmion is able to traverse the high-anisotropy region and exhibits Shapiro steps with constant values of $\langle v_x \rangle$. On these steps, the ac driving frequency resonates with the rate at which the skyrmion is crossing the periodic substrate pattern. When $j_{ac} > j_{dc}$, the system remains locked on a single step and there are only small oscillations around the velocities of $\langle v_x \rangle \approx 5$ m/s and $\langle v_y \rangle \approx 14$ m/s. This behavior is more like what would be expected for a Kapitza pendulum [15,90,91], where the width of the locking steps grows monotonically with increasing ac drive amplitude rather than oscillating as in the case of Shapiro steps.

In Figs. 9(a) and 9(b) we illustrate the skyrmion trajectories for the system in Fig. 8(a) at $j_{ac} = 2.05 \times 10^{10}$ A m^{-2} and $j_{ac} = 5.89 \times 10^{10}$ A m^{-2}, respectively. The plot of θ_{sk} versus j_{ac} in Fig. 8(b) indicates that the average direction of skyrmion motion remains locked to $\theta_{sk} \approx 69^\circ$ over the entire range of j_{ac} values considered here. Similarly to the behavior shown in Sec. III, the skyrmion traverses the high-anisotropy regions during the positive portion of the ac drive cycle. In Fig. 9(a) the skyrmion traverses one stripe during the $+x$ portion of the ac drive cycle and is displaced only slightly along $-x$ during the $-x$ portion of the ac drive cycle due to the low amplitude of the ac drive. In the Supplemental Material [87], we show this skyrmion trajectory in a short animation. When the ac drive amplitude is larger, as in Fig. 9(b), the skyrmion moves *backwards* by one stripe during the $-x$ portion of the ac drive cycle. The interaction of the skyrmion with the barrier at the $R_L - R_H$ interface changes during each portion of the drive cycle. An animation of this trajectory can be found in the Supplemental Material [87]. For the $+x$ portion of the cycle, the skyrmion tends to slide along the $-y$ direction, while during the $-x$ portion of the cycle it slides along the $+y$ direction. This behavior enables the skyrmion to jump over the barrier during the $-x$ portion of the ac drive cycle and therefore causes the average skyrmion velocity to remain constant as long as $j_{ac} > j_{dc}$, as shown in Fig. 8(a).

Figure 8(c) shows $\langle v_x \rangle$ and $\langle v_y \rangle$ versus j_{ac} for samples in which both the ac and dc driving is applied along the x direction, and Fig. 8(d) shows the corresponding θ_{sk} versus j_{ac} curve. As illustrated by the trajectories in Figs. 9(c) and 9(d), for this drive orientation the skyrmion exhibits a very orderly transport process. Since both driving currents are applied along the same direction, the dc drive biases the ac driving cycle and alternately enhances or reduces the effective

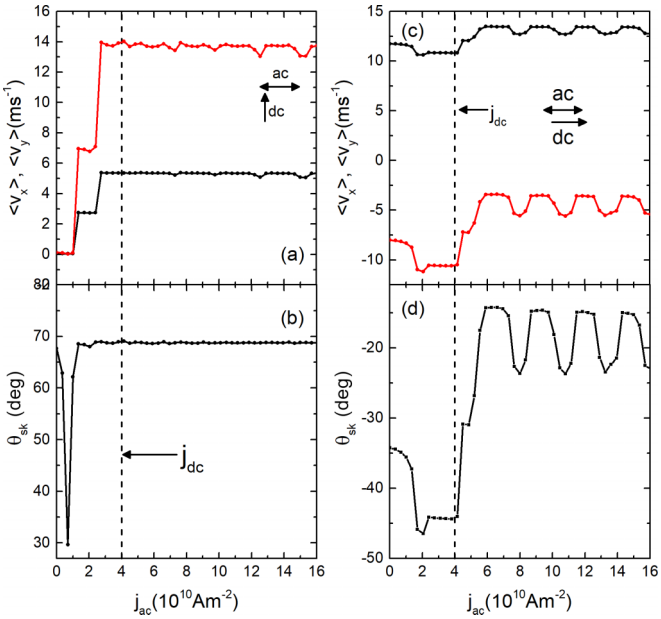

FIG. 8. [(a) and (c)] $\langle v_x \rangle$ (black) and $\langle v_y \rangle$ (red) vs j_{ac} and [(b) and (d)] θ_{sk} vs j_{ac} for samples with fixed $j_{dc} = 4 \times 10^{10}$ A m^{-2} and $D/J = 0.18$. [(a) and (b)] ac drive applied along the x direction and dc drive applied along the $+y$ direction. [(c) and (d)] ac and dc drives applied along the x direction. The vertical dashed lines indicate the point at which $j_{ac} = j_{dc}$.

ac driving force, making it easier or harder, respectively, for the skyrmion to cross the $R_L - R_H$ barriers. As j_{ac} increases for fixed j_{dc}, the velocities pass through a series of constant velocity Shapiro steps produced by resonances between the ac drive frequency and the rate at which the skyrmion moves across the periodic potential. Unlike the case for ac driving that is perpendicular to the dc drive, the skyrmion direction of motion for parallel drives is not locked in a specific direction, but changes as a function of j_{ac}, as shown in Fig. 8(d).

The motion of the system in Fig. 8(c) is illustrated in Fig. 9(c) at $j_{ac} = 3.10 \times 10^{10}$ A m^{-2}, where the skyrmion follows a zigzag trajectory. As the skyrmion crosses from R_L to R_H, it translates slightly along $-y$, while when it crosses from R_H back to R_L, it moves slightly along $+y$ due to the interaction with the $R_L - R_H$ interface. Transport between stripes only occurs during the $+x$ portion of the ac drive cycle. During the $-x$ portion of the ac drive cycle, the skyrmion cannot overcome the $R_L - R_H$ barrier due to the reduction in skyrmion velocity produced by the $+x$ dc drive. Although the net force is still along $+x$ since $j_{dc} > j_{ac}$, it is not strong enough to push the skyrmion across the potential barrier, and instead the skyrmion only slides along $-y$. At $j_{ac} = 6.95 \times 10^{10}$ A m^{-2} in Fig. 9(d), the net force on the skyrmion is in the $-x$ direction during the $-x$ portion of the ac drive cycle since $j_{ac} > j_{dc}$. Nevertheless, it is still not large enough to push the skyrmion over the potential barrier along the $-x$ direction, resulting in a fast sliding motion of the skyrmion along the $+y$ direction. The skyrmion can only surpass the potential barrier during the $+x$ portion of the ac drive cycle, when both the ac and dc drives combine to push the skyrmion towards the $+x$ direction with great force, causing the skyrmion to translate to the right by a distance of nine stripes.

V. SKYRMION INSTABILITY AND FUTURE DIRECTIONS

We find that a range of D/J values exists in which, instead of well-defined skyrmions that produce Shapiro steps, an instability arises that transforms the skyrmion into an elongated magnetic texture. The instability always occurs when the skyrmion is crossing from the high-anisotropy region to the lower-anisotropy region, $R_H \rightarrow R_L$. It is important to note that in this situation, the size of the skyrmion is increasing as the crossing occurs. The skyrmion size is smaller in higher-anisotropy regions and larger in lower-anisotropy regions. In Figs. 10(a)–10(d), we illustrate the time evolution of the transformation of a skyrmion into an elongated magnetic texture at $D/J = 0.51$. We observe very similar results for the range $0.51 < D/J < 0.85$. When $D/J \approx 1$, the skyrmion is usually very small, and smaller skyrmions tend to be more stable. Additionally, when the skyrmion radius becomes very small, variations in the skyrmion radius when passing from one anisotropy region to another also become quite small, so no instability can arise. Outside of the instability window, a stable skyrmion can pass from the high-anisotropy to low-anisotropy region without distorting in shape, as illustrated in Figs. 10(e)–10(h) for $D/J = 0.45$. When the instability occurs, it can become quite extensive and can result in an expansion of the skyrmion into shapes similar to that shown in Fig. 10(i). The instability may arise due to a velocity difference in the skyrmion motion in the two regions which causes a portion of the skyrmion to expand outward. This instability will be addressed in greater detail in a future work to better understand the topological transition. For example, it could also occur for simpler sample geometries containing only a single interface between regions of different anisotropy. Another question is how important the ac driving is to producing the instability.

VI. DISCUSSION

There are many possible future directions for this system, such as considering multiple skyrmions, exploring the effect of adding a magnetic field, inclusion of finite temperature, or considering nonadiabatic effects in the STT current. In the case of multiple skyrmions, collective effects would play a major role and could produce either collective transport of all skyrmions or a plastic flow regime in which a portion of the skyrmions are moving while the rest of the skyrmions remain pinned. The collective interaction of skyrmions at the interface could also result in distinctive annihilation effects. The inclusion of a finite temperature could cause creep motion at small currents, shift the locations of the depinning and dynamic transitions, and even modify the conditions for skyrmion stabilization [92]. One of the most prominent effects of introducing a nonadiabatic STT is that it would alter the skyrmion Hall angle and the depinning current [79,93]. Thus, the addition of nonadiabatic contributions could alter the conditions for the skyrmion crossing the interface from R_L to R_H, where the skyrmion is repelled from the high-anisotropy region.

We note that the PMA has a significant impact on the system. If the PMA is too strong, then the energy required to move the skyrmion across the stripes would become so high

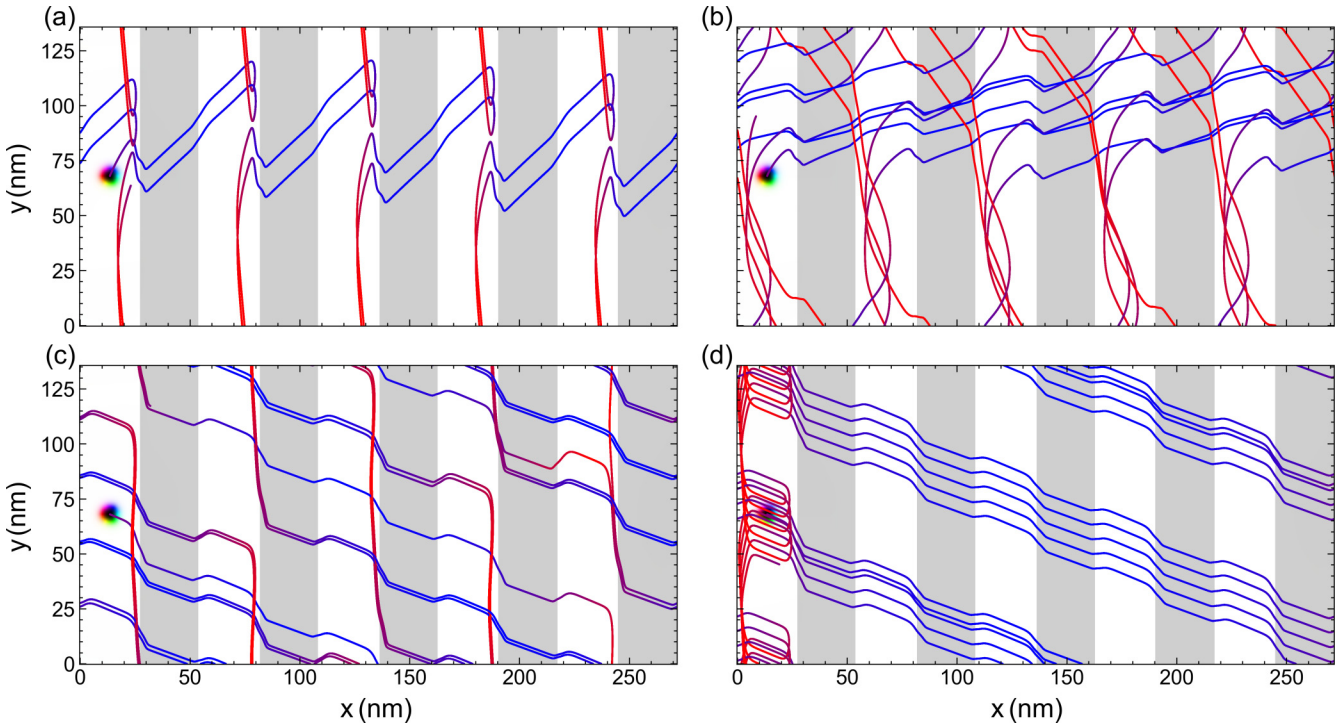

FIG. 9. Skyrmion trajectories for systems with $j_{dc} = 4.0 \times 10^{10}$ A m^{-2}, $D/J = 0.18$, and ac driving applied along the x direction. The trajectory color varies as a gradient from blue to red corresponding to the $+y$ and $-y$ portion of the ac driving cycle, respectively. White stripes represent lower-anisotropy regions and gray stripes indicate higher-anisotropy regions. [(a) and (b)] dc driving applied along the $+y$ direction with (a) $j_{ac} = 2.05 \times 10^{10}$ A m^{-2} and (b) $j_{ac} = 5.89 \times 10^{10}$ A m^{-2}. [(c) and (d)] dc driving applied along the $+x$ direction with (c) $j_{ac} = 3.10 \times 10^{10}$ A m^{-2} and (d) $j_{ac} = 6.95 \times 10^{10}$ A m^{-2}.

that it would destroy the skyrmion itself, so the PMA constant K_H should be controlled carefully. The ac drive frequency is also crucial. If the frequency is too high, then it could impede the skyrmion motion across interfaces, since the skyrmion requires sufficient time to respond to the combined dc and ac driving forces.

We focused on a one-dimensional modulation of the anisotropy, but similar effects could occur for skyrmions moving over periodic substrates that have two-dimensional variations. If some asymmetry, such as a sawtooth gradient, were introduced to the stripes, then various ratchet effects could appear. Here we only considered the case of orthogonal dc and ac drives; however, other configurations, such as diagonal dc and ac currents, could also be explored. In this scenario, we expect the Shapiro steps to be modulated by the angle between the ac and dc drives, with robust Shapiro steps appearing for orthogonal currents and sparse steps for acute angles. Additionally, the dc drive could be replaced by another ac drive. In this case, the synchronization of the ac drives could lead to additional transport behaviors, with motion regimes and static phases that are modulated by the phase difference and ac drive frequencies. In addition to skyrmions, it would be interesting to study whether similar Shapiro step phenomena could arise for antiskyrmions, merons, and bimerons. It should also be possible to use the Shapiro step phenomenon to create new devices that require the skyrmions to be moved at specific velocities or over specific distances.

From an experimental perspective, possible methods for creating the sample considered here include using periodic thickness modulations [94], patterning the sample with stripes of irradiation [95,96], or employing a VCMA technique [76,77].

VII. SUMMARY

Using atomistic simulations, we simulate the dynamical behavior of a single skyrmion interacting with an array of stripes of different anisotropy under a combination of external ac and dc driving. When a fixed ac drive is applied along the y direction and a dc drive of varied amplitude is applied along the $+x$ direction, the average velocity passes through a series of Shapiro steps. On each step, $\langle v_x \rangle$ is constant but $\langle v_y \rangle$ increases in magnitude with increasing dc drive amplitude, and there is a jump down in $\langle v_y \rangle$ at the transition between adjacent Shapiro steps. The skyrmion Hall angle or angle of skyrmion motion changes across each step, and the skyrmion trajectories on each step are distinct. We show that the Shapiro steps only appear when $j_{dc} \leqslant j_{ac}$, indicating that j_{ac} controls the number of Shapiro steps that can be observed. Increasing j_{ac} increases the number of Shapiro steps that are present until a saturation value is reached, above which the Shapiro step behavior is lost. By varying D/J, we vary the size of the skyrmion, and find that this quantity does not play a major role in determining the appearance of the Shapiro steps, although it does change the sharpness of the transition between adjacent Shapiro steps as well as the shape of the skyrmion trajectories. For lower values of D/J the transitions are sharp, but on increasing D/J, the transitions start to become more continuous. We expect that for high values of D/J, such as $D/J = 1$, the Shapiro steps will vanish and be replaced by an

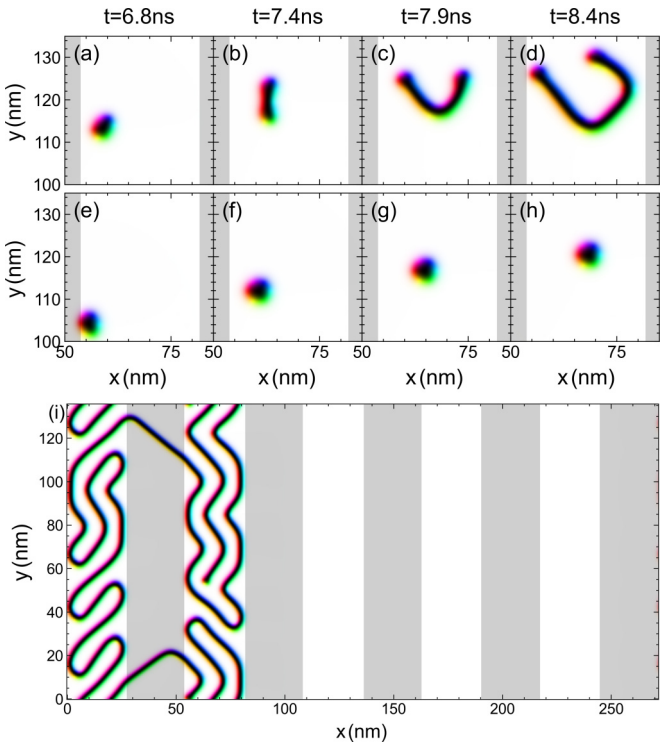

FIG. 10. Snapshots from systems with $j_{dc} = 1 \times 10^{10}$ A m^{-2} and $j_{ac} = 5 \times 10^{10}$ A m^{-2}. [(a)–(d)] In a system with $D/J = 0.51$, the skyrmion deforms due to instabilities arising during the transition from a high-anisotropy region (gray) to a low-anisotropy region (white). [(e)–(h)] In a system with $D/J = 0.45$, the same transition from a high-anisotropy region to a low-anisotropy region does not cause any distortion or instability of the skyrmion. (i) The final simulated configuration of the $D/J = 0.51$ system from panels (a)–(d) showing the appearance of a "magnetic worm" after the deformation instability. Note that both ends of the worm are in the same low-anisotropy stripe, with one end in the lower middle of the stripe and the other end at the very top of the stripe.

almost linear relationship between the skyrmion velocity and the magnitude of the dc drive.

We also show that different combinations of dc and ac driving directions can lead to different skyrmion behavior. When the dc drive is fixed along the $+y$ direction and a varying perpendicular ac drive is applied along the x direction, the skyrmion direction of motion is locked and θ_{sk} remains constant, but Shapiro velocity steps appear. When the ac drive amplitude is higher than the dc drive magnitude, the system remains locked along a single direction. For the case of ac and dc drives both applied along the x direction, we find oscillations in the average skyrmion velocity associated with positive and negative contributions of the ac drive cycle to the dc drive. Our results confirm many of the results previously observed in particle-based models of skyrmions and show that Shapiro step phenomena for various combinations of driving direction should be a robust feature in skyrmion systems. The results presented here can be used to control the motion of skyrmions by taking advantage of the Shapiro steps and sinusoidal behaviors observed for different combinations of external applied drives.

ACKNOWLEDGMENTS

This work was supported by the U.S. Department of Energy through the Los Alamos National Laboratory. Los Alamos National Laboratory is operated by Triad National Security, LLC, for the National Nuclear Security Administration of the U. S. Department of Energy (Contract No. 892333218NCA000001). J.C.B.S. acknowledges funding from Fundação de Amparo à Pesquisa do Estado de São Paulo—FAPESP (Grant No. 2022/14053-8). We thank Dr. Felipe F. Fanchini for providing the computational resources used in this work. These resources were funded by the Fundação de Amparo à Pesquisa do Estado de São Paulo - FAPESP (Grant No. 2021/04655-8).

[1] A. Pikovsky, M. Rosenblum, and J. Kurths, *Synchronization: A Universal Concept in Nonlinear Sciences: 12* (Cambridge University Press, Cambridge, UK, 2003).

[2] E. Ott, *Chaos in Dynamical Systems*, 2nd ed. (Cambridge University Press, Cambridge, UK, 2002).

[3] M. Bennett, M. F. Schatz, H. Rockwood, and K. Wiesenfeld, Huygens's clocks, Proc. R. Soc. Lond. A **458**, 563 (2002).

[4] L. Glass, Synchronization and rhythmic processes in physiology, Nature (London) **410**, 277 (2001).

[5] S. Shapiro, Josephson currents in superconducting tunneling: The effect of microwaves and other observations, Phys. Rev. Lett. **11**, 80 (1963).

[6] A. Barone and G. Paterno, *Physics and Applications of the Josephson Effect*, 1st ed. (Wiley-VCH, New York, 1982).

[7] S. P. Benz, M. S. Rzchowski, M. Tinkham, and C. J. Lobb, Fractional giant Shapiro steps and spatially correlated phase motion in 2D Josephson arrays, Phys. Rev. Lett. **64**, 693 (1990).

[8] S. N. Coppersmith and P. B. Littlewood, Interference phenomena and mode locking in the model of deformable sliding charge-density waves, Phys. Rev. Lett. **57**, 1927 (1986).

[9] G. Grüner, The dynamics of charge-density waves, Rev. Mod. Phys. **60**, 1129 (1988).

[10] S. E. Brown, G. Mozurkewich, and G. Grüner, Subharmonic Shapiro steps and devil's-staircase behavior in driven charge-density-wave systems, Phys. Rev. Lett. **52**, 2277 (1984).

[11] P. Martinoli, O. Daldini, C. Leemann, and E. Stocker, A.C. quantum interference in superconducting films with periodically modulated thickness, Solid State Commun. **17**, 205 (1975).

[12] P. Martinoli, Static and dynamic interaction of superconducting vortices with a periodic pinning potential, Phys. Rev. B **17**, 1175 (1978).

[13] O. V. Dobrovolskiy, AC quantum interference effects in nanopatterned Nb microstrips, J. Supercond. Nov. Magn. **28**, 469 (2015).

[14] L. Van Look, E. Rosseel, M. J. Van Bael, K. Temst, V. V. Moshchalkov, and Y. Bruynseraede, Shapiro steps in a

superconducting film with an antidot lattice, Phys. Rev. B **60**, R6998 (1999).
[15] C. Reichhardt, R. T. Scalettar, G. T. Zimányi, and N. Grønbech-Jensen, Phase-locking of vortex lattices interacting with periodic pinning, Phys. Rev. B **61**, R11914 (2000).
[16] I. Sokolović, P. Mali, J. Odavić, S. Radošević, S. Yu. Medvedeva, A. E. Botha, Y. M. Shukrinov, and J. Tekić, Devil's staircase and the absence of chaos in the dc- and ac-driven overdamped Frenkel-Kontorova model, Phys. Rev. E **96**, 022210 (2017).
[17] J. Tekić and Z. Ivić, Frequency dependence of the subharmonic Shapiro steps, Phys. Rev. E **83**, 056604 (2011).
[18] M. P. N. Juniper, A. V. Straube, R. Besseling, D. G. A. L. Aarts, and R. P. A. Dullens, Microscopic dynamics of synchronization in driven colloids, Nat. Commun. **6**, 7187 (2015).
[19] T. Brazda, C. July, and C. Bechinger, Experimental observation of Shapiro-steps in colloidal monolayers driven across time-dependent substrate potentials, Soft Matter **13**, 4024 (2017).
[20] J. L. Abbott, A. V. Straube, D. G. A. L. Aarts, and R. P. A. Dullens, Transport of a colloidal particle driven across a temporally oscillating optical potential energy landscape, New J. Phys. **21**, 083027 (2019).
[21] C. Reichhardt, A. B. Kolton, D. Domínguez, and N. Grønbech-Jensen, Phase-locking of driven vortex lattices with transverse ac force and periodic pinning, Phys. Rev. B **64**, 134508 (2001).
[22] V. I. Marconi, A. B. Kolton, D. Domínguez, and N. Grønbech-Jensen, Transverse phase locking in fully frustrated Josephson junction arrays: A different type of fractional giant steps, Phys. Rev. B **68**, 104521 (2003).
[23] C. Reichhardt, C. J. Olson, and M. B. Hastings, Rectification and phase locking for particles on symmetric two-dimensional periodic substrates, Phys. Rev. Lett. **89**, 024101 (2002).
[24] C. Reichhardt and C. J. Olson Reichhardt, Absolute transverse mobility and ratchet effect on periodic two-dimensional symmetric substrates, Phys. Rev. E **68**, 046102 (2003).
[25] J. Tekić, A. E. Botha, P. Mali, and Y. M. Shukrinov, Inertial effects in the dc + ac driven underdamped Frenkel-Kontorova model: Subharmonic steps, chaos, and hysteresis, Phys. Rev. E **99**, 022206 (2019).
[26] N. Nagaosa and Y. Tokura, Topological properties and dynamics of magnetic skyrmions, Nat. Nanotechnol. **8**, 899 (2013).
[27] S.-G. Je, H.-S. Han, S. K. Kim, S. A. Montoya, W. Chao, I.-S. Hong, E. E. Fullerton, K.-S. Lee, K.-J. Lee, M.-Y. Im, and J.-I. Hong, Direct demonstration of topological stability of magnetic skyrmions *via* topology manipulation, ACS Nano **14**, 3251 (2020).
[28] C. J. Olson Reichhardt, S. Z. Lin, D. Ray, and C. Reichhardt, Comparing the dynamics of skyrmions and superconducting vortices, Physica C **503**, 52 (2014).
[29] C. Reichhardt and C. J. Olson Reichhardt, Depinning and nonequilibrium dynamic phases of particle assemblies driven over random and ordered substrates: A review, Rep. Prog. Phys. **80**, 026501 (2017).
[30] C. Reichhardt, C. J. O. Reichhardt, and M. V. Milošević, Statics and dynamics of skyrmions interacting with disorder and nanostructures, Rev. Mod. Phys. **94**, 035005 (2022).
[31] K. Litzius, I. Lemesh, B. Krüger, P. Bassirian, L. Caretta, K. Richter, F. Büttner, K. Sato, O. A. Tretiakov, J. Förster, R. M. Reeve, M. Weigand, I. Bykova, H. Stoll, G. Schütz, G. S. D. Beach, and M. Kläui, Skyrmion Hall effect revealed by direct time-resolved x-ray microscopy, Nat. Phys. **13**, 170 (2017).
[32] J. Iwasaki, M. Mochizuki, and N. Nagaosa, Universal current-velocity relation of skyrmion motion in chiral magnets, Nat. Commun. **4**, 1463 (2013).
[33] W. Jiang, X. Zhang, G. Yu, W. Zhang, X. Wang, M. B. Jungfleisch, J. E. Pearson, X. Cheng, O. Heinonen, K. L. Wang, Y. Zhou, A. Hoffmann, and S. G. E. te Velthuis, Direct observation of the skyrmion Hall effect, Nat. Phys. **13**, 162 (2017).
[34] S.-Z. Lin, C. Reichhardt, C. D. Batista, and A. Saxena, Driven skyrmions and dynamical transitions in chiral magnets, Phys. Rev. Lett. **110**, 207202 (2013).
[35] S.-Z. Lin, C. Reichhardt, C. D. Batista, and A. Saxena, Particle model for skyrmions in metallic chiral magnets: Dynamics, pinning, and creep, Phys. Rev. B **87**, 214419 (2013).
[36] K. Zeissler, S. Finizio, C. Barton, A. J. Huxtable, J. Massey, J. Raabe, A. V. Sadovnikov, S. A. Nikitov, R. Brearton, T. Hesjedal, G. van der Laan, M. C. Rosamond, E. H. Linfield, G. Burnell, and C. H. Marrows, Diameter-independent skyrmion Hall angle observed in chiral magnetic multilayers, Nat. Commun. **11**, 428 (2020).
[37] A. Fert, N. Reyren, and V. Cros, Magnetic skyrmions: Advances in physics and potential applications, Nat. Rev. Mater. **2**, 17031 (2017).
[38] C. Reichhardt, D. Ray, and C. J. Olson Reichhardt, Quantized transport for a skyrmion moving on a two-dimensional periodic substrate, Phys. Rev. B **91**, 104426 (2015).
[39] C. Reichhardt, D. Ray, and C. J. O. Reichhardt, Nonequilibrium phases and segregation for skyrmions on periodic pinning arrays, Phys. Rev. B **98**, 134418 (2018).
[40] J. Feilhauer, S. Saha, J. Tobik, M. Zelent, L. J. Heyderman, and M. Mruczkiewicz, Controlled motion of skyrmions in a magnetic antidot lattice, Phys. Rev. B **102**, 184425 (2020).
[41] N. P. Vizarim, J. C. B. Souza, C. Reichhardt, C. J. O. Reichhardt, and P. A. Venegas, Directional locking and the influence of obstacle density on skyrmion dynamics in triangular and honeycomb arrays, J. Phys.: Condens. Matter **33**, 305801 (2021).
[42] N. P. Vizarim, C. Reichhardt, C. J. O. Reichhardt, and P. A. Venegas, Skyrmion dynamics and topological sorting on periodic obstacle arrays, New J. Phys. **22**, 053025 (2020).
[43] C. Reichhardt and C. J. O. Reichhardt, Commensuration effects on skyrmion Hall angle and drag for manipulation of skyrmions on two-dimensional periodic substrates, Phys. Rev. B **105**, 214437 (2022).
[44] V. L. Carvalho-Santos, M. A. Castro, D. Salazar-Aravena, D. Laroze, R. M. Corona, S. Allende, and D. Altbir, Skyrmion propagation along curved racetracks, Appl. Phys. Lett. **118**, 172407 (2021).
[45] A. Korniienko, A. Kákay, D. D. Sheka, and V. P. Kravchuk, Effect of curvature on the eigenstates of magnetic skyrmions, Phys. Rev. B **102**, 014432 (2020).
[46] K. V. Yershov, A. Kákay, and V. P. Kravchuk, Curvature-induced drift and deformation of magnetic skyrmions: Comparison of the ferromagnetic and antiferromagnetic cases, Phys. Rev. B **105**, 054425 (2022).
[47] N. P. Vizarim, C. Reichhardt, P. A. Venegas, and C. J. O. Reichhardt, Guided skyrmion motion along pinning array interfaces, J. Magn. Magn. Mater. **528**, 167710 (2021).

[48] C.-L. Zhang, J.-N. Wang, C.-K. Song, N. Mehmood, Z.-Z. Zeng, Y.-X. Ma, J.-B. Wang, and Q.-F. Liu, Edge-guided heart-shaped skyrmion, Rare Metals **41**, 865 (2022).

[49] C. Reichhardt, D. Ray, and C. J. O. Reichhardt, Magnus-induced ratchet effects for skyrmions interacting with asymmetric substrates, New J. Phys. **17**, 073034 (2015).

[50] J. C. B. Souza, N. P. Vizarim, C. J. O. Reichhardt, C. Reichhardt, and P. A. Venegas, Skyrmion ratchet in funnel geometries, Phys. Rev. B **104**, 054434 (2021).

[51] W. Chen, L. Liu, Y. Ji, and Y. Zheng, Skyrmion ratchet effect driven by a biharmonic force, Phys. Rev. B **99**, 064431 (2019).

[52] B. Göbel and I. Mertig, Skyrmion ratchet propagation: Utilizing the skyrmion Hall effect in AC racetrack storage devices, Sci. Rep. **11**, 3020 (2021).

[53] J. C. Bellizotti Souza, N. P. Vizarim, C. J. O. Reichhardt, C. Reichhardt, and P. A. Venegas, Controlled skyrmion ratchet in linear protrusion defects, Phys. Rev. B **109**, 054407 (2024).

[54] R. Yanes, F. Garcia-Sanchez, R. F. Luis, E. Martinez, V. Raposo, L. Torres, and L. Lopez-Diaz, Skyrmion motion induced by voltage-controlled in-plane strain gradients, Appl. Phys. Lett. **115**, 132401 (2019).

[55] S. L. Zhang, W. W. Wang, D. M. Burn, H. Peng, H. Berger, A. Bauer, C. Pfleiderer, G. van der Laan, and T. Hesjedal, Manipulation of skyrmion motion by magnetic field gradients, Nat. Commun. **9**, 2115 (2018).

[56] K. Everschor, M. Garst, B. Binz, F. Jonietz, S. Mühlbauer, C. Pfleiderer, and A. Rosch, Rotating skyrmion lattices by spin torques and field or temperature gradients, Phys. Rev. B **86**, 054432 (2012).

[57] L. Kong and J. Zang, Dynamics of an insulating skyrmion under a temperature gradient, Phys. Rev. Lett. **111**, 067203 (2013).

[58] X. Gong, H. Y. Yuan, and X. R. Wang, Current-driven skyrmion motion in granular films, Phys. Rev. B **101**, 064421 (2020).

[59] N. Del-Valle, J. Castell-Queralt, L. González-Gómez, and C. Navau, Defect modeling in skyrmionic ferromagnetic systems, APL Mater. **10**, 010702 (2022).

[60] H. Y. Yuan, X. S. Wang, M.-H. Yung, and X. R. Wang, Wiggling skyrmion propagation under parametric pumping, Phys. Rev. B **99**, 014428 (2019).

[61] X. Zhang, Y. Zhou, M. Ezawa, G. P. Zhao, and W. Zhao, Magnetic skyrmion transistor: Skyrmion motion in a voltage-gated nanotrack, Sci. Rep. **5**, 11369 (2015).

[62] L. Zhao, X. Liang, J. Xia, G. Zhao, and Y. Zhou, A ferromagnetic skyrmion-based diode with a voltage-controlled potential barrier, Nanoscale **12**, 9507 (2020).

[63] R. M. Menezes, J. F. S. Neto, C. C. de Souza Silva, and M. V. Milošević, Manipulation of magnetic skyrmions by superconducting vortices in ferromagnet-superconductor heterostructures, Phys. Rev. B **100**, 014431 (2019).

[64] J. F. Neto and C. C. de Souza Silva, Mesoscale phase separation of skyrmion-vortex matter in chiral-magnet–superconductor heterostructures, Phys. Rev. Lett. **128**, 057001 (2022).

[65] X. Zhang, J. Xia, and X. Liu, Structural transition of skyrmion quasiparticles under compression, Phys. Rev. B **105**, 184402 (2022).

[66] J. C. Bellizotti Souza, N. P. Vizarim, C. J. O. Reichhardt, C. Reichhardt, and P. A. Venegas, Spontaneous skyrmion conformal lattice and transverse motion during dc and ac compression, New J. Phys. **25**, 053020 (2023).

[67] X. Zhang, J. Xia, O. A. Tretiakov, M. Ezawa, G. Zhao, Y. Zhou, X. Liu, and M. Mochizuki, Laminar and transiently disordered dynamics of magnetic-skyrmion pipe flow, Phys. Rev. B **108**, 144428 (2023).

[68] N. P. Vizarim, J. C. Bellizotti Souza, C. J. O. Reichhardt, C. Reichhardt, M. V. Milošević, and P. A. Venegas, Soliton motion in skyrmion chains: Stabilization and guidance by nanoengineered pinning, Phys. Rev. B **105**, 224409 (2022).

[69] J. C. B. Souza, N. P. Vizarim, C. J. O. Reichhardt, C. Reichhardt, and P. A. Venegas, Soliton motion induced along ferromagnetic skyrmion chains in chiral thin nanotracks, J. Magn. Magn. Mater. **587**, 171280 (2023).

[70] H. Du, D. Song, W. Wang, S. Zhang, N. Wang, F. Zheng, M. Tian, R. Dunin-Borkowski, and J. Zang, Steady motion of 80-nm-size skyrmions in a 100-nm-wide track (unpublished).

[71] C. Liu, J. Wang, W. He, C. Zhang, S. Zhang, S. Yuan, Z. Hou, M. Qin, Y. Xu, X. Gao, Y. Peng, K. Liu, Z. Q. Qiu, J.-M. Liu, and X. Zhang, Strain-induced reversible motion of skyrmions at room temperature, ACS Nano **18**, 761 (2024).

[72] X. Xing and Y. Zhou, Skyrmion motion and partitioning of domain wall velocity driven by repulsive interactions, Commun. Phys. **5**, 241 (2022).

[73] C. Reichhardt and C. J. Olson Reichhardt, Shapiro steps for skyrmion motion on a washboard potential with longitudinal and transverse ac drives, Phys. Rev. B **92**, 224432 (2015).

[74] C. Reichhardt and C. J. Olson Reichhardt, Shapiro spikes and negative mobility for skyrmion motion on quasi-one-dimensional periodic substrates, Phys. Rev. B **95**, 014412 (2017).

[75] N. P. Vizarim, C. Reichhardt, P. A. Venegas, and C. J. O. Reichhardt, Shapiro steps and nonlinear skyrmion Hall angles for dc and ac driven skyrmions on a two-dimensional periodic substrate, Phys. Rev. B **102**, 104413 (2020).

[76] B. Dai, M. Jackson, Y. Cheng, H. He, Q. Shu, H. Huang, L. Tai, and K. Wang, Review of voltage-controlled magnetic anisotropy and magnetic insulator, J. Magn. Magn. Mater. **563**, 169924 (2022).

[77] B. Rana and Y. C. Otani, Towards magnonic devices based on voltage-controlled magnetic anisotropy, Commun. Phys. **2**, 90 (2019).

[78] R. F. L. Evans, "Atomistic spin dynamics," in *Handbook of Materials Modeling: Applications: Current and Emerging Materials*, edited by W. Andreoni and S. Yip (Springer International, Cham, 2018), pp. 1–23.

[79] J. Iwasaki, M. Mochizuki, and N. Nagaosa, Current-induced skyrmion dynamics in constricted geometries, Nat. Nanotechnol. **8**, 742 (2013).

[80] S. Paul, S. Haldar, S. von Malottki, and S. Heinze, Role of higher-order exchange interactions for skyrmion stability, Nat. Commun. **11**, 4756 (2020).

[81] S. Seki and M. Mochizuki, *Skyrmions in Magnetic Materials* (Springer International, Cham, 2016).

[82] J. C. Slonczewski, Dynamics of magnetic domain walls, AIP Conf. Proc. **5**, 170 (1972).

[83] T. L. Gilbert, A phenomenological theory of damping in ferromagnetic materials, IEEE Trans. Magn. **40**, 3443 (2004).

[84] J. Zang, M. Mostovoy, J. H. Han, and N. Nagaosa, Dynamics of skyrmion crystals in metallic thin films, Phys. Rev. Lett. **107**, 136804 (2011).

[85] T. Schulz, R. Ritz, A. Bauer, M. Halder, M. Wagner, C. Franz, C. Pfleiderer, K. Everschor, M. Garst, and A. Rosch, Emergent electrodynamics of skyrmions in a chiral magnet, Nat. Phys. **8**, 301 (2012).

[86] O. Boulle, J. Vogel, H. Yang, S. Pizzini, D. de Souza Chaves, A. Locatelli, T. O. Menteş, A. Sala, L. D. Buda-Prejbeanu, O. Klein, M. Belmeguenai, Y. Roussigné, A. Stashkevich, S. M. Chérif, L. Aballe, M. Foerster, M. Chshiev, S. Auffret, I. M. Miron, and G. Gaudin, Room-temperature chiral magnetic skyrmions inultrathin magnetic nanostructures, Nat. Nanotechnol. **11**, 449 (2016).

[87] See Supplemental Material at http://link.aps.org/supplemental/10.1103/PhysRevB.110.014406 for further description of videos. It exhibits animation videos of skyrmion trajectories for selected cases with complex trajectories.

[88] R. Juge, K. Bairagi, K. G. Rana, J. Vogel, M. Sall, D. Mailly, V. T. Pham, Q. Zhang, N. Sisodia, M. Foerster, L. Aballe, M. Belmeguenai, Y. Roussigné, S. Auffret, L. D. Buda-Prejbeanu, G. Gaudin, D. Ravelosona, and O. Boulle, Helium ions put magnetic skyrmions on the track, Nano Lett. **21**, 2989 (2021).

[89] J. C. B. Souza, N. P. Vizarim, C. J. O. Reichhardt, C. Reichhardt, and P. A. Venegas, Clogging, diode and collective effects of skyrmions in funnel geometries, New J. Phys. **24**, 103030 (2022).

[90] L. D. Landau and E. M. Lifshitz, *Mechanics*, 3rd ed. (Pergamon, Oxford, 1976).

[91] C. Reichhardt and C. J. Olson, Transverse phase locking for vortex motion in square and triangular pinning arrays, Phys. Rev. B **65**, 174523 (2002).

[92] A. Sonntag, J. Hermenau, S. Krause, and R. Wiesendanger, Thermal stability of an interface-stabilized skyrmion lattice, Phys. Rev. Lett. **113**, 077202 (2014).

[93] X. Zhang, J. Xia, G. P. Zhao, X. Liu, and Y. Zhou, Magnetic skyrmion transport in a nanotrack with spatially varying damping and non-adiabatictorque, IEEE Trans. Magn. **53**, 1 (2017).

[94] A. Hierro-Rodriguez, M. Vélez, R. Morales, N. Soriano, G. Rodríguez-Rodríguez, L. M. Àlvarez Prado, J. I. Martín, and J. M. Alameda, Controlled nucleation of topological defects in the stripe domain patterns of lateral multilayers with perpendicular magnetic anisotropy, Phys. Rev. B **88**, 174411 (2013).

[95] M. Abes, J. Venuat, D. Muller, A. Carvalho, G. Schmerber, E. Beaurepaire, A. Dinia, and V. Pierron-Bohnes, Magnetic patterning using ion irradiation for highly ordered CoPt alloys with perpendicular anisotropy, J. Appl. Phys. **96**, 7420 (2004).

[96] D. Makarov, S. Tibus, C. T. Rettner, T. Thomson, B. D. Terris, T. Schrefl, and M. Albrecht, Magnetic strip patterns induced by focused ion beam irradiation, J. Appl. Phys. **103**, 063915 (2008).